Pulsar lensing geometry

Siqi Liu[1,3]⋆, Ue-Li Pen[1,2,4]†, J-P Macquart[5]‡, Walter Brisken[6]§, Adam Deller[7]¶

[1] *Canadian Institute for Theoretical Astrophysics, University of Toronto, M5S 3H8 Ontario, Canada*
[2] *Canadian Institute for Advanced Research, Program in Cosmology and Gravitation*
[3] *Department of Astronomy and Astrophysics, University of Toronto, M5S 3H4, Ontario, Canada*
[4] *Dunlap Institute for Astronomy & Astrophysics, University of Toronto, M5S 3H4, Ontario, Canada*
[5] *ICRAR-Curtin University of Technology, Department of Imaging and Applied Physics, GPO Box U1978, Perth, Western Australia 6102, USA*
[6] *National Radio Astronomy Observatory, P.O. Box O, Socorro, NM 87801, USA*
[7] *ASTRON, the Netherlands Institute for Radio Astronomy, Postbus 2, 7990 AA, Dwingeloo, The Netherlands*

4 February 2016

ABSTRACT

We test the inclined sheet pulsar scintillation model (Pen & Levin 2014) against archival VLBI data on PSR 0834+06 and show that its scintillation properties can be precisely reproduced by a model in which refraction occurs on two distinct lens planes. These data strongly favour a model in which grazing-incidence refraction instead of diffraction off turbulent structures is the primary source of pulsar scattering. This model can reproduce the parameters of the observed diffractive scintillation with an accuracy at the percent level. Comparison with new VLBI proper motion results in a direct measure of the ionized ISM screen transverse velocity. The results are consistent with ISM velocities local to the PSR 0834+06 sight-line (through the Galaxy). The simple 1-D structure of the lenses opens up the possibility of using interstellar lenses as precision probes for pulsar lens mapping, precision transverse motions in the ISM, and new opportunities for removing scattering to improve pulsar timing. We describe the parameters and observables of this double screen system. While relative screen distances can in principle be accurately determined, a global conformal distance degeneracy exists that allows a rescaling of the absolute distance scale. For PSR B0834+06, we present VLBI astrometry results that provide (for the first time) a direct measurement of the distance of the pulsar. For most of the recycled millisecond pulsars that are the targets of precision timing observations, the targets where independent distance measurements are not available. The degeneracy presented in the lens modelling could be broken if the pulsar resides in a binary system.

Key words: Pulsars: individual (B0834+06) – scattering – waves – magnetic: reconnection – techniques: interferometric – ISM: structure

1 INTRODUCTION

Pulsars have long provided a rich source of astrophysical information due to their compact emission and predictable timing. One of the least well-constrained parameters for most pulsars is their distance. For some pulsars, timing or VLBI parallax has resulted in direct distance determination. For most pulsars, the distance is a major uncertainty for precision timing interpretations, including mass, moment of

inertia (Kramer et al. 2006; Lorimer & Kramer 2012), and gravitational wave direction (Boyle & Pen 2012).

Direct VLBI observations of PSR B0834+06 show multiple images lensed by the interstellar plasma. Combining the angular positions and scintillation delays, the authors (Brisken et al. 2010) (hereafter B10) published the derived effective distance (defined in Section 3.1) of 1168 ± 23 pc for apexes on the main scattering axis. This represents a precise measurement compared to all other attempts to derive distances to this pulsar. This effective distance is a combination of pulsar-screen and earth-screen distances, and does not allow a separate determination of the individual distances. A binary pulsar system would in principle allow a breaking of this degeneracy (Pen & Levin 2014). One potential lim-

⋆ E-mail: sqliu@cita.utoronto.ca
† E-mail: pen@cita.utoronto.ca
‡ E-mail: J.Macquart@curtin.edu.au
§ Email: wbrisken@aoc.nrao.edu
¶ E-mail: deller@astron.nl

itation is the precision to which the lensing model can be understood.

In this paper, we examine the geometric nature of the lensing screens. The first hints of a single-plane collinear-dominated structure had been realized in Stinebring et al. (2001). In B10, VLBI astrometric mapping directly demonstrated the highly collinear nature of a single dominant lensing structure. While the nature of these structures is already mysterious, for this pulsar, in particular, the puzzle is compounded by an offset group of lenses whose radiation arrive delayed by 1-ms relative to the bulk of the pulsar flux. The mysterious nature of the lensing questions any conclusions drawn from scintillometry as a quantitative tool (Pen et al. 2014).

Using archival data we demonstrate in this paper that the lensing screen consists of nearly parallel linear refractive structures, in two screens. The precise model fits the one dimensional nature of the scattering geometry, and thus the small number of parameters that quantify the lensing screen.

The paper is structured as follows. Section 2 presents new VLBI proper motion and distance measurements to this pulsar. Section 3 is an overview of the inclined sheet lensing model and its application to data. Section 4 describes the interpretation of the lensing geometry and possible improvements on the observation. We conclude in Section 5.

2   VLBI ASTROMETRY

In order to eliminate the degeneracies inherent in lens modelling, we undertook an astrometric VLBI program to measure the distance and transverse velocity of PSR B0834+06.

PSR B0834+06 was observed 8 times with the Very Long Baseline Array (VLBA), under the project code BB269, between 2009 May and 2011 January. Four 16 MHz bands spread across the frequency range 1406 – 1692 MHz were sampled with 2 bit quantization in both circular polarizations, giving a total data rate of 512 Mbps per antenna. The primary phase calibrator was J0831+0429, which is separated from the target by 2.1 degrees, but the target field also included an in-beam calibrator source J083646.4+061108, which is separated from PSR B0834+06 by only 5 ′. The cycle time between primary phase calibrator and target field was 5 minutes, and the total duration of each observation was 4 hours.

Standard astrometric data reduction techniques were applied (e.g., Deller et al. 2012, 2013), using a phase calibration solution interval of 4 minutes for the in-beam calibrator source J083646.4+061108. J083646.4+061108 is weak (flux density ∼4 mJy) and its brightness varied on the level of tens of percent. The faintness leads to noisy solutions, and the variability indicates that source structure evolution (which would translate to offsets in the fitted target position) could be present. Together, these two effects lead to reduced astrometric precision compared to that usually obtained with VLBI astrometry using in-beam calibration, and the results presented here could be improved upon if the observations were repeated using the wider bandwidths and higher sensitivity now available with the VLBA, potentially in conjunction with additional in-beam background sources.

While a straightforward fit to the astrometric observables yields a pulsar distance with a formal error <1 per

Table 1. Fitted and derived astrometric parameters for PSR B0834+06.

Reference right ascension (J2000)[a]	08:37:5.644606(9)
Reference declination (J2000)[a]	06:10:15.4047(1)
Position epoch (MJD)	55200
$\mu_{R.A.}$ (mas yr^{-1})	2.16(19)
μ_{Dec} (mas yr^{-1})	51.64(13)
Parallax (mas)	1.63(15)
Distance (pc)	620(60)
v_T (km s^{-1})	150(15)

[a] The errors quoted here are from the astrometric fit only and do not include the ∼1 mas position uncertainty transferred from the in–beam calibrator's absolute position.

cent, the reduced χ^2 of this fit is ∼40, indicating that the formal position errors greatly underestimate the true position errors, and that systematic effects such as the calibrator effects discussed above as well as residual ionospheric errors dominate. Accordingly, the astrometric parameters and their errors were instead obtained by bootstrap sampling (Efron & Tibshirani 1991). These results are presented in Table 1.
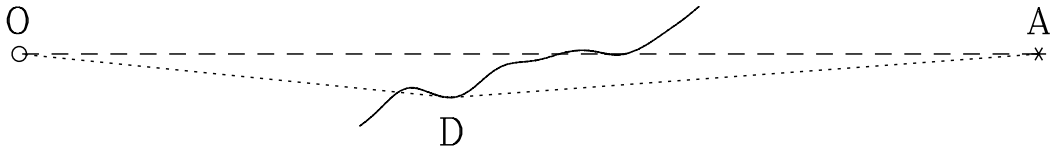
3   LENSING

In this section, we map the archival VLBI data of PSR 0834+06 onto the grazing incidence sheet model. The folded sheet model is qualitatively analogous to the reflection of a light across a lake as seen from the opposite shore. In the absence of waves, exactly one image forms at the point where the angle of incidence is equal to the angle of reflection. In the presence of waves, one generically sees a line of images above and below the unperturbed image. The grazing angle geometry simplifies the lensing geometry, effectively reducing it from a two dimensional problem to one dimension. The statistics of such reflections is sometimes called glitter, and has many solvable properties (Longuet-Higgins 1960). This is illustrated in Fig. 1.

A similar effect occurs when the observer is below the surface. Two major distinctions arise: 1. the waves can deform the surface to create caustics in projection. Near caustics, Snell's law can lead to highly amplified refraction angles (Goldreich & Sridhar 2006). 2. due to the odd image theorem, each caustic leads to two additional images, more specifically, 1(original) + 2 × n(additional images for n caustics) = 2n + 1 (total images we observe is odd). In an astrophysical context, the surface could be related to magnetic reconnection sheets (Braithwaite 2015), which have finite widths to regularize these singularities. Diffusive structures have Gaussian profiles, which were analysed in Pen & King (2012). The lensing details differ for convergent (under-dense) vs divergent (over-dense) lenses, first considered by Clegg et al. (1998).

The typical interstellar electron density ∼ 0.02 cm^{-3} is insufficient to deflect radio waves by the observed ∼ mas bending angles. At grazing incidence, Snell's law results in an enhanced bending angle, which formally diverges. Magnetic discontinuities generically allow transverse surface waves, whose restoring force is the difference in Alfvén speed on the two sides of the discontinuity. This completes the analogy to waves on a lake: for sufficiently inclined sheets

Figure 1. Reflection of lights on surface waves. At grazing angle, each wave crest results in an apparent image, causing a linear streak of images centred on the unperturbed image location. For example, the red light streak would consist of a single image at its center in the absence of waves. The inclined sheet model for pulsar scintillation is analogous, with reflection replaced by refraction. Image copyright Kaitlyn McLachlan, licensed through shutterstock.com image ID 45186139.


Figure 2. Refractive lensing geometry (reproduced from Pen & Levin (2014) fig. 1). The pulsar is on the right, observer on the left. Each fold of the sheet leads to a divergent projected density, resulting in a lensed image as indicated by the dotted line. See text for details.

the waves will appear to fold back onto themselves in projection on the sky. At each fold caustic, Snell's law diverges, leading to enhanced refractive lensing. The divergence is cut off by the finite width of the sheet. The generic consequence is a series of collinear images. Each projected fold of the wave results in two density caustics. Each density caustic leads to two geometric lensing images, for a total of 4 images for each wave inflection. The two geometric images in each caustic are separated by the characteristic width of the sheet. If this is smaller than the Fresnel scale, the two images become effectively indistinguishable. The geometry of

the inclined refractive lens is shown in Fig. 2. A detailed view of the light path near the fold point D is illustrated in Fig. 3.

A large number of sheets might intersect the line of sight to any pulsar. Only those sufficiently inclined would lead to caustic formation. Empirically, some pulsars show scattering that appears to be dominated by a single sheet, leading to the prominent inverted arclets in the secondary spectrum of the scintillations (Stinebring et al. 2001). The secondary spectrum analysis, specifically, $P(f_\nu, f_t) = |S^\dagger(f_\nu, f_t)|^2$, which $\dagger$ stands for the 2-D Fourier transform, f_ν is the con-
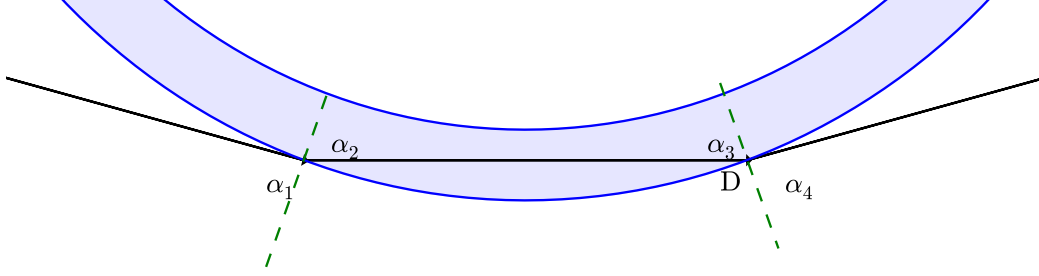
Figure 3. Refraction of light rays near point D. The black lines are the light paths. The shaded region indicates the lensing sheet caustic. The angles obey Snell's Law $\sin(\alpha_1)/\sin(\alpha_2) = \sin(\alpha_4)/\sin(\alpha_3) = n_{\mathrm{ISM}}/n_{\mathrm{sheet}}$.

jugate frequency and f_t is the conjugate time. $S(\nu, t)$ is the measurement of flux density as a function of frequency and time, which maps the information of the differential time and differential frequency of different rays of the pulsar (Hill et al. 2003; Walker et al. 2004; Cordes et al. 2006).

3.1   Archival data of B0834+06

Our analysis is based on the apex data selected from the secondary spectrum of pulsar B0834+06 in B10, which was observed as part of a 300 MHz global VLBI project on 2005 November 12, with the GBT (GB), Arecibo (AR), Lovell and Westerbork (WB) telescopes. The GB-AR and AR-WB baselines are close to orthogonal and of comparable lengths, resulting in relatively isotropic astrometric positions. Information from each identified apex includes delay τ, delay rate (differential frequency f_D), relative right ascension, $\Delta\alpha$, and relative declination, $\Delta\delta$. Data of each apex are collected from four dual circular polarization 8 MHz wide sub-bands spanning the frequency range 310.5–342.5 MHz. As described in B10, the inverse parabolic arclets were fitted to positions of their apexes, resulting in a catalogue of apexes in each sub-band, each with delay and differential frequency. In this work, we first combine the apexes across sub-bands, resulting in a single set of images. We focus on the southern group with negative differential frequency: this grouping appears as a likely candidate for a double-refraction screen. However, two groups (with negative differential frequency) appear distinct in both the VLBI angular positions and the secondary spectra. We divide the apex data with negative f_D into two groups: in one group, time delays range from 0.1 ms to 0.4 ms, which we call the 0.4-ms group; and in the other group, time delay at about 1 ms, which we call the 1-ms group. In summary, the 0.4-ms group contains 10 apexes in the first two sub-bands, and 14 apexes in the last two sub-bands; the 1-ms group, contains 5, 6, 5 and 4 apexes in the four sub-bands. Four bands are with center frequency $f_{\mathrm{band}} = 314.5, 322.5, 330.5$ and 338.5 MHz. The apex positions in the secondary spectrum are shown in Fig. 4, in band centred at 330.5 MHz. The 1-ms and 0.4-ms groups are marked separately in Fig. 4.

We select the equivalent apexes from four sub-bands. To match the same apexes in different sub-bands, we scale the differential frequency in different sub-bands to 322.5 MHz.
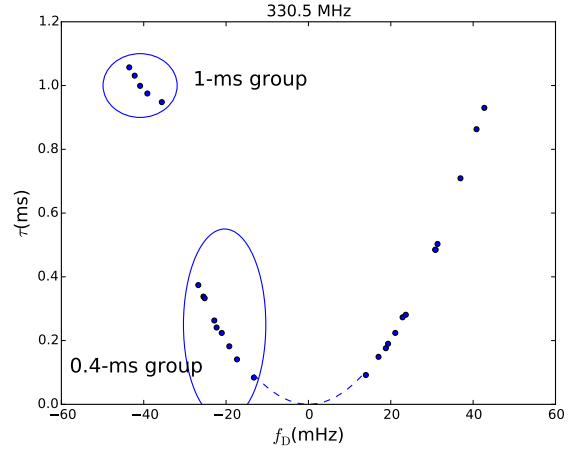
Figure 4. A schematic of the distribution of a subset of apex positions in the secondary spectrum of the scintillations in the sub-band centred on 330.5 MHz. The apexes that belong to the 1-ms and 0.4-ms groups are marked.

We use Eq. 1,

$$f_{\mathrm{Dref}} = f_D(322.5 \text{ MHz}/f_{\mathrm{band}}), \qquad (1)$$

where f_{Dref} is the re-scaled differential frequency centred at 322.5 MHz, f_D is the original differential frequency of each apex, f_{band} is the center frequency of each sub-bands. The the radio frequency scaling of the arc apex positions and arc curvature in secondary spectrum are illustrated in Hill et al. (2003). A total of 9 apexes from the 0.4-ms group and 5 apexes from the 1-ms group, are mapped. This is displayed with the mean referenced frequency $f = 322.5$ MHz and a standard deviation among the sub-bands, listed in Table 2. The τ, f_D, $\Delta\alpha$ and $\Delta\delta$ are the mean values of n sub-bands ($n = 3$ for points 4 to 6 and points 1', 2' and 4', while 4 for the remainder of the points), listed in Table 2.

We estimate :

$$\sigma_{\mathrm{band}}^2 = \frac{1}{n-1}\sum_{i=1}^{n}(x_i - \bar{x})^2, \qquad (2)$$

$$\sigma_{\mathrm{apex}}^2 = \frac{\sigma_{\mathrm{band}}^2}{n}, \qquad (3)$$

where the σ_{band} is the standard deviation of each sub-bands, the σ_{band} is the error of the mean of n sub-bands and n is

label	$\theta_\parallel$ (mas)	f_D (mHz)	τ (ms)	$\Delta\alpha$ (mas)	$\Delta\delta$ (mas)	t_0 (day)
1	-17.22	$-26.1(4)$	$0.3743(6)$	6.2	-11.9	-107
2	-16.36	$-24.9(4)$	$0.3378(3)$	$8.0(4)$	$-14.5(8)$	-101
3	-16.08	$-24.6(4)$	$0.327(3)$	$7.2(6)$	$-13.9(4)$	-99.0
4	-14.45	$-22.3(5)$	$0.2633(3)$	$6.1(4)$	$-13.1(7)$	-88.1
5	-13.68	$-21.2(6)$	$0.236(2)$	$5.1(4)$	$-12.7(5)$	-81.8
6	-13.27	$-20.4(5)$	$0.222(3)$	$5.8(4)$	$-11.8(1)$	-81.4
7	-12.21	$-18.9(2)$	$0.188(2)$	$5.5(6)$	$-10.8(6)$	-74.2
8	-10.58	$-16.8(3)$	$0.1412(9)$	$3.9(6)$	$-10.0(4)$	-62.8
9	-8.18	$-12.9(2)$	$0.0845(5)$	$2.8(3)$	$-8.6(4)$	-48.7
1'	$\cdots$	$-43.1(4)$	$1.066(5)$	$-8(3)$	$-24(2)$	-185
2'	$\cdots$	$-41.3(5)$	$1.037(3)$	$-14(1)$	$-23(3)$	-188
3'	$\cdots$	$-40.2(6)$	$1.005(8)$	$-14(1)$	$-22.3(5)$	-187
4'	$\cdots$	$-38.3(6)$	$0.9763(9)$	$-14(1)$	$-20.6(3)$	-190
5'	$\cdots$	$-35.1(5)$	$0.950(2)$	$-15(1)$	$-21(1)$	-202

Table 2. 0.4-ms and 1-ms reduced apex data, with reference frequency 322.5 MHz. We list the 0.4-ms group data in the upper part of the table, while the 1-ms group lie in the lower part of the table. Data in the second column mark the fitted result of the angular offset from the θ and $\sqrt{\tau}$ relation in Fig. 6 and the time delays in column four. Observation data include the differential frequency f_D (in the frequency band centred at 322.5 MHz), time delay τ (τ_1 for 0.4-ms group and τ_2 for 1-ms group); $\Delta\alpha$ and $\Delta\delta$ are from the VLBI measurement (there is only one matched position for point 1, thus no error). t_0 is the time at constant velocity for an apex to intersect the origin at constant speed along the main scattering parabola. More details in Section 3.1 and Section 3.2.2.

Table 3. Parameters for double-refraction model

D_{1e}	Effective Distance of 0.4 group data
D_{2e}	Effective Distance of 1-ms group data
D_1	Distance of lens 1
D_2	Distance of lens 2
α_i	Angles of incidence and refraction near point D[a]
γ	Scattering axis angle of 0.4-ms group[b]
ϕ	Angle of the velocity of the pulsar[b]
θ	Angular offset of the object

[a] i=1,2,3,4. 1 and 3 are for the incidence angles, while 2 and 4 are for the refraction angles.
[b] The angle is measured relative to the longitude and east is the positive direction.

Figure 5. A single refracted light path showing the distance degeneracy. The primed and un-primed geometries result in the same observables: delay τ and angular offset θ. O denotes the observer; A and A' denote the positions of the pulsar; D and D' denote the positions of the refracted images on the interstellar medium. The un-primed geometry corresponds to a pulsar distance $D_p = |AO| = 620$ pc, while the primed geometry has the same D_e but twice the D_p.

the number of sub-bands. For each apex, the error of time delay τ, differential frequency f_D, $\Delta\alpha$ and $\Delta\delta$ are listed in Table 2 from their band-to-band variance.

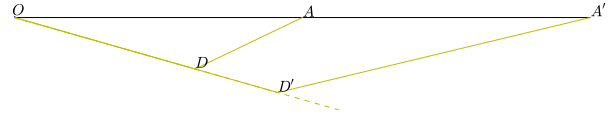## 3.2 Single-refraction model

3.2.1 Distance to the lenses

In the absence of a lens model, the fringe rate, delay and angular position cannot be uniquely related. To interpret the data, we adopt the lensing model of Pen & Levin (2014). In this model, the lensing is due to projected fold caustics of a thin sheet closely aligned to the line of sight. We will list the parameters in this lens model in Table 3.
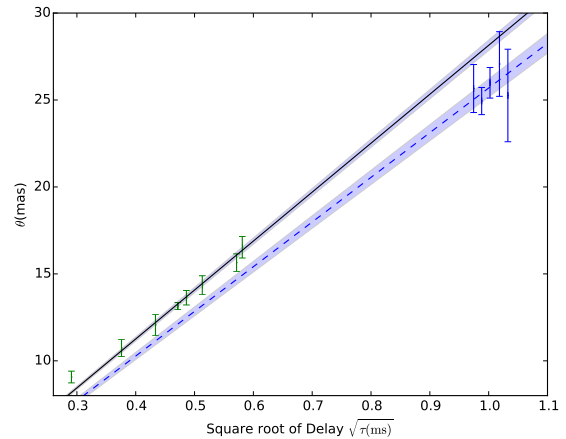
We define the *effective distance* D_e as

$$D_e \equiv \frac{2c\tau}{\theta^2}. \tag{4}$$

The differential frequency is related to the rate of change of delay as $f_D = -f\frac{d\tau}{dt}$. In general, $D_e = D_p D_s/(D_p - D_s)$ for a screen at D_s. The effective distance corresponds to the pulsar distance D_p, if the screen is exactly halfway. Fig. 5 shows two sets of D_p and D_s with common D_e.

When estimating the angular offset of each apex, we

Figure 6. θ vs $\sqrt{\tau}$. Two separate lines through the origin are fitted to the points sampled among the 0.4-ms group and 1-ms group. The solid line is the fitted line of the 0.4-ms positions, where $D_{1e} = 1044 \pm 22$ pc. The dashed line is the fitted line of the 1-ms position, where $D_{2e} = 1252 \pm 49$ pc.

subtract the expected noise bias: $\theta^2 = (\Delta\alpha\cos(\delta))^2 + (\Delta\delta)^2 - \sigma^2_{\Delta\alpha} - \sigma^2_{\Delta\delta}$. We plot the θ vs square root of τ in Fig. 6. A least-square fit to the distance results in $D_{1e} = 1044 \pm 22$ pc for the 0.4-ms group, which we call lens 1 (point 1 is excluded since VLBI astrometry is only known for one sub-band, thus we cannot obtain the variance nor weighted mean for that point), and $D_{2e} = 1252 \pm 49$ pc for the 1-ms group, hereafter lens 2. The errors, and uncertainties on the error, preclude a definitive interpretation of the apparent difference in distance. However, at face value, this indicates that lens 2 is closer to the pulsar, and we will use this as a basis for the model in this paper. The distances are slightly different from those derived in B10, which is partly due to a different subset of arclets analysed. We discuss consequences of alternate interpretations in Section 3.4. As shown in Section 2, the pulsar distance has been independently measured to be $D_p = 620 \pm 60$ pc. The distance of lens 1, where the group of scintillation points with 0.4-ms delays are refracted, is $D_1 = 389$ pc, as we take $D_{1e} = 1044$ pc. Similarly, for 1-ms apexes, the distance of lens 2 is taken as $D_2 = 415$ pc, slightly closer to the pulsar.

For the 0.4-ms group, we adopt the geometry from B10, assigning these points along line AD as shown in Fig. 7 based solely on their delay, which is the best-measured observable. The sky-projected direction of the line AD is taken as a fixed angle of $\gamma = -25°.2$ east north. We use this axis to define the $\parallel$ direction; then the $\perp$ direction is rotated $90°$ clockwise.

3.2.2   Discussion of single-refraction model

The 0.4-ms group lens solution appears consistent with the premise of the inclined sheet lensing model (Pen & Levin 2014), which predicts collinear positions of lensing images. The time in the last column of Table 2, which we denote as $t_0 = -2\tau f/f_D$, corresponds to the time required for the arclet to drift in the secondary spectrum through a delay of zero.

The collinearity can be considered a post-diction of this model. The precise positions of each image are random, and with 9 images no precision test is possible. The predictive power of the sheet model becomes clear in the presence of a second, off-axis screen, which will be discussed in Section 3.3.

3.2.3   Why is the 1-ms feature simply not single scattering due to a second screen?

Scattering from a second, highly inclined screen would result in a second parabolic arc in the secondary spectrum, which go through the same origin but with different curvature. We can conclude from Fig. 4 that this does not agree with the data.

Furthermore, in this scenario, referring to Fig. 5 in B10, the loci of the arclets on the sky should point back to the pulsar (the origin), according to Pen & Levin (2014), which also does not agree with the observation results.

3.3   Double-refraction model

The apparent offset of the 1-ms group can be explained by refraction through two lens screens. The small number of apexes at 1-ms suggests that the second lens screen involves a single caustic at a different distance. One expects each lens to re-image the full set of first scatterings, resulting in a number of apparent images equal to the product of number of lenses in each screen. In the primary lens system, the inclination appears such that typical waves form caustics. For the sake of discussion, we consider an inclination angle for lens 1 $\iota_1 = 0.1°$, and a typical slope of waves $\sigma_\iota = \iota_1$. Each wave of gradient larger than 1-σ will form a caustic in projection. The number of sheets at shallower inclination increases as the square of this small angle. A 3 times less-inclined $\iota_2 = 0.3°$ sheet occurs 9 times as often. For the same amplitude waves on this second surface, they only form caustics for 3-σ waves, which occur two hundred times less often. Thus, one expects such sheets to only form isolated caustics, which we expect to see occasionally. Three free parameters describe a second caustic: distance, angle, and angular separation. We fix the distances from the effective VLBI distance (D_1 and D_2), and fit the angular separations and angles with the 5 delays of the 1-ms group.

3.3.1   Solving the double-refraction model

Apexes 1'–5' share a similar 1-ms time delay, suggesting they are lensed by a common structure. We denote the position of the pulsar point as point A, the positions of the lensed image on lens 2 as point H, positions of the lensed image on lens 1 as point B, position of the observer as point O, and the nearest point on lens 2 to the pulsar as point J. The lines $AJ \perp HJ$ intersect at point J, $HF \perp BD$ intersect at the points F, and $BG \perp HJ$ intersect at the points G.

A 3-D schematic of two plane lensing by linear caustics is shown in Fig. 8.

First, we calculate the position of J. We estimate the distance of J from the 1-ms θ–$\sqrt{\tau}$ relation (see Fig. 6). We determine the position of J by matching the time delays of point 4' and point 1', which is marked in Fig. 7. The long dash dotted line on the right side of Fig. 7 denotes the inferred geometry of lens 2, and by construction perpendicular to AJ.

The second step is to find the matched pairs of those two lenses. By inspection, we find that the 5 furthest points in 0.4-ms group match naturally to the double-refraction images. These five matched lines are marked with cyan dash dotted lines in Fig. 7 and their values are listed in the second column in Table 4. They are the located at a distance 389 pc away from us. Here we define three distances:

$$D_{p2} = 620 \text{ pc} - 415 \text{ pc} = 205 \text{ pc},$$
$$D_{21} = 415 \text{ pc} - 389 \text{ pc} = 26 \text{ pc}, \tag{5}$$

where D_{p2} is the distance from the pulsar to lens 2, and D_{21} is the distance from lens 2 to lens 1.

Fig. 9 and Fig. 10 are examples of how light is refracted on the first lens plane and the second lens plane. We specifically choose the point with $\theta_\parallel = -17.22$ mas, which refer point 1' on lens 1 as an example. Equality of the velocity of the photon parallel to the lens plane before and after refrac-
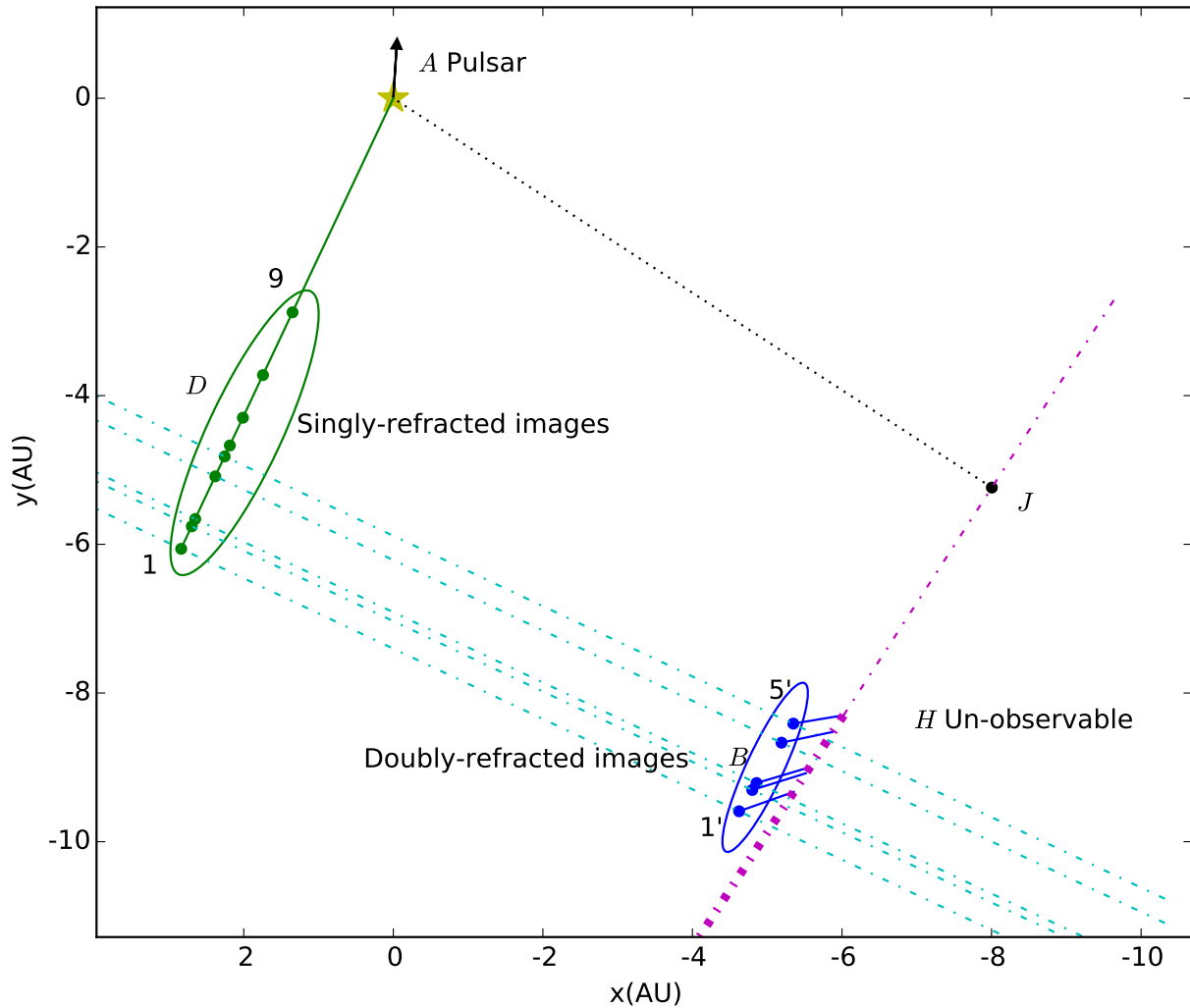
Figure 7. Positions of 0.4-ms and 1-ms group data in the single-refraction model and double-refraction model. The axes represent the relative transverse distances to the un-refracted pulsar in right ascension (calculated by $x = \Delta\alpha\cos(\delta)D_i$ with D_i represent the distance of the object to the observer: for point A, $D_i = D_\mathrm{p}$; for points H and J, $D_i = D_2$; for points B and D, $D_i = D_1$.) and declination (calculated by $y = \Delta\delta D_i$) directions, on a 2-D plane that is transverse to the line of sight. On the left side, the points marked with letter D labelled from 1 to 9, are the derived positions from the time delays of 0.4-ms group in the single-refraction model. At a distance 389 pc from the observer, the green solid line demarcates the scattering axis for the 0.4-ms apexes positions, with an angle $\gamma = -25°.2$ east of north. The points on the right side mark the first and second refraction points in the double-refraction model. The unobservable points denoted by the letter H, are the calculated positions on lens 2 from the 1-ms group; the observed apparent positions denoted by the letter B, are the second refraction on lens 1. They are connected by short solid lines. The long dash dotted line passing through J is the inferred geometry of the second lens. Its thicker portion has formed a full caustic, while the thinner portion are sub critical. The dash dotted lines, constructed perpendicular to the AD scattering axis, denote the caustics of lens 1. The dotted line on the top right is perpendicular to the magenta dash dotted line, intersecting at J. The relative model pulsar-screen velocity is 185.3 km s^{-1}, with an angle $\phi = -3°.7$ east of north, is marked with an arrow from the star, at point A, at the top of the figure.
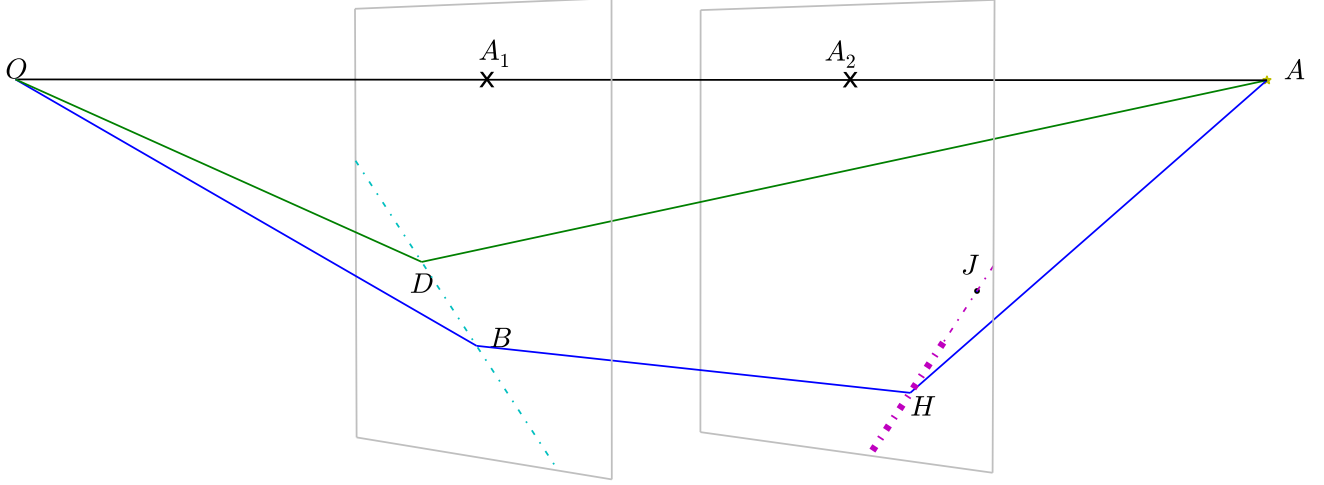
Figure 8. A 3-D schematic of light path when light is doubly-refracted. Two planes from left to right are the plane of lens 1, and the plane of lens 2. Light (the blue solid line) goes from A (pulsar) to the first refracted point H on lens 2 (line HJ, magenta dash dotted line), and then the second refracted point B, the image we observe, on lens 1 (line BD, cyan dash dotted line), and finally the observer O. The green solid line shows the light path of singly-deflected light path ($A - D - O$). The crosses (A_1 on plane 1, and A_2 on plane 2) denote intersection of the un-deflected light through the lensing sheet. D and J are the closest point of the lens caustic to the un-deflected path, which are the loci of single deflection images. Thus, $A_2J\perp HJ$, and $A_1D\perp BD$. The dash dotted lines represent the projected line-like fold caustics of the two lenses. The thick dash dotted line on plane 2 indicates the real caustic, while the thin continuation indicates the extrapolated continuation beyond the cusp/swallowtail.

label	$\theta_\parallel$ (mas)	τ_2(ms)	σ_τ(ms)	τ_M(ms)	f_D(mHz)	σ_f(mHz)	f_M(mHz)	t_1(day)
1'	−17.22	1.0663	0.0050	1.0663*	−43.08	0.84	−42.26	−78
2'	−16.36	1.0370	0.0059	1.0362	−41.27	0.88	−41.04	−73
3'	−16.08	1.005	0.011	1.027	−40.17	0.87	−40.64	−72
4'	−14.45	0.9763	0.00088	0.9763*	−38.31	0.64	−38.31†	−63
5'	−13.68	0.9495	0.0094	0.9550	−35.06	0.78	−37.21	−59

Table 4. Comparison of time delay τ and the differential frequency f_D (with reference frequency 322.5 MHz) of the observation and the model fitting result in the double-refraction model. $\theta_\parallel$ denotes the angular offsets of the corresponding images at lens 1. The values with asterisks on them are the points that we use to calculate the position of J and the point with a † symbol is the point that we use to calculate the transverse velocity of the pulsar $v_\perp$. They agree with data by construction. The last column, t_1 is the time the lensed image on lens 2 takes to move from point H to point J, which is defined in Section 3.3.3.

tion implies the relation:

$$\frac{JH}{D_{p2}} = \frac{HG}{D_{21}},$$
$$\frac{FB}{D_{21}} = \frac{BD}{D_1}. \tag{6}$$

We plot the solved positions in Fig. 7, and list respective time delays and differential frequencies in Table 4. We take the error of the time delay τ in the double-refraction model as

$$\left(\frac{\sigma_{\tau i}}{\tau_{2i}}\right)^2 = \left(\frac{\sigma_{\tau 1i}}{\tau_{1i}}\right)^2 + \left(\frac{\sigma_{\tau 2i}}{\tau_{2i}}\right)^2 + \left(\frac{\sigma_{\tau 2j}}{\tau_{2j}}\right)^2, \tag{7}$$

where τ_1 and $\sigma_{\tau 1}$ represent the time delay and its error from the 0.4-ms group on lens 1, and τ_2 and $\sigma_{\tau 2}$ represent the time delay and its error from the 1-ms group on lens 2. And τ_{2j} is the τ_2 for the nearest reference point in Table 4 with error $\sigma_{\tau 2j}$. Specifically, for point $i = 5'$ and $3'$, $j = 4'$ is the nearest reference point; while for point $i = 2'$, $j = 1'$ is the nearest reference point. The reference points are marked with star symbols in the fifth column in Table 4.

For the error of differential frequency f_D, we add the error of the reference point (point 4') to the error of each
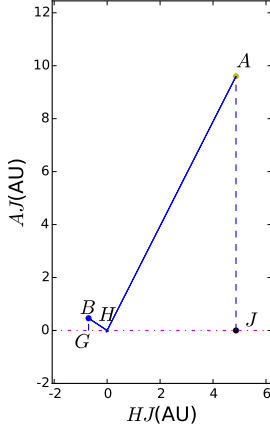
Figure 9. Refraction on lens 2. A is the position of the pulsar. H is the lensed image on lens 2. B is the lensed image on lens 1. $AJ \perp HJ$ and $BG \perp HJ$. We illustrate the scenario for point 1'.
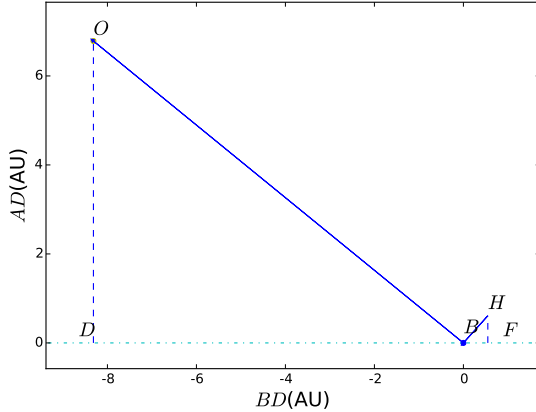
Figure 10. Refraction on lens 1. H is the lensed image on lens 2. B is the lensed image on lens 1. O is the position of the observer. $HF \perp DF$ and $OD \perp HJ$. As in the previous figure, we illustrate the scenario for point 1'.

other measured point:

$$\left(\frac{\sigma_{f_i}}{f_{\mathrm{D}i}}\right)^2 = \left(\frac{\sigma_{f_{\mathrm{D}i}}}{f_{\mathrm{D}i}}\right)^2 + \left(\frac{\sigma_{f_{\mathrm{D}4'}}}{f_{\mathrm{D}4'}}\right)^2 \tag{8}$$

where $f_{\mathrm{D}4'}$ and $\sigma_{f_{\mathrm{D}4'}}$ are the differential frequency of point $4'$ and its error. We marked this point with † symbol in the fourth row in Table 4.

3.3.2 Comparing with observations

In order to compare τ, we calculate model time delays τ_{M} for these five points, and list the results in Table 4. For points 4' and 1', they fit by construction since we use these to calculate the position of J; for the remaining three points, all of the results are within 3-σ of the observed time delays.

To compare differential frequency f_{D}, we need to calculate the velocity of the pulsar and the velocity of the lens. We take the lenses to be static, and solve the velocity of the

pulsar relative to the lens (in geocentric coordinates). The pulsar has two velocity components, and the two 1-D lenses effectively determine one component each. For $v_\parallel$, we derive the velocity 172.4 ± 2.4 km s^{-1}, which is 58.7 mas/yr in a geocentric system, from f_{D} of point 1-ms in 0.4-ms group. The direct observable is the time to crossing of each caustic, denoted t_0 in Table 2.

To calculate $v_\perp$, we choose the point 4', which has the smallest errorbar of differential frequency. This gives a value of 67.9 ± 2.8 km s^{-1} for $v_\perp$, which is 21.4 mas/yr in geocentric system, with an angle $\phi = -3°.7 \pm 0°.8$ west of north. This represents the pulsar-screen velocity relative to the Earth. We can further transform this into the local standard of rest (LSR) frame to interpret the velocities in a Galactic context. The model derived and observed velocities (heliocentric and LSR) are listed in Table 5. The direction of the model velocity is marked on the top of the star in Fig. 7.

With this velocity of the pulsar, we calculate the model differential frequency f_{M} of points 5',3',2' and 1'. Results are listed in Table 4. The calculated results all lie within the 3-σ error intervals of the observed data.

The reduced χ^2 for time delay τ is 1.5 for 3 degrees of freedom and 2.2 for f_{D} for 4 degrees of freedom. This is consistent with the model.

Within this lensing model, we can test if the caustics are parallel. Using the lag error range of double-lensed point 4 (the best constrained), we find a 1-σ allowed angle of 0.4 degrees from parallel with the whole lensing system. This lends support to the hypothesis of a highly inclined sheet, probably aligned to better than 1 per cent.

### 3.3.3 Discussion of double-refraction model

For the 1-ms group, lens 2 only images a subset of the lens 1 images. This could happen if the lens 1 screen is just under the critical inclination angle, such that only 3-σ waves lead to a fold caustic. If the lens 2 was at a critical angle, the chance of encountering a somewhat less inclined system is of order unity. More surprising is the absence of a singly-refracted image of the pulsar, which is expected at position J. This could happen if the maximum refraction angle is just below critical, such that only rays on the appropriately aligned double refraction can form images. We plot the refraction angle β in the direction that is transverse to the first lens plane in Fig. 11. The fractional bandwidth of the data is about 10 per cent, making it unlikely that single lens image J would not be seen due to the larger required refraction angle. Instead, we speculate that the fold caustic terminates near double-refracted image 5', and thus only intersections with the closer lens plane caustic south of image 5' are doubly-refracted.

This is a generic outcome of a swallowtail catastrophe (Arnold 1990). In this picture, the sheet just starts folding near point 5'. North of point 5', no fold appears in projection. Far south of point 5', a full fold exhibits two caustics emanating from the fold cusp. Near the cusp the magnification is the superposition of two caustics, leading to enhanced lensing and higher likelihood of being observed.

We denote t_1 the time for the lensed image on lens 2 to move from point H to point J. From our calculation, we predict that on 2005 September 14, which is 59 days before the observation, the lensed image would have appeared

Parameter	$\mu_{\alpha*}$(mas yr^{-1})	μ_{δ}(mas yr^{-1})	μ_{l*}(mas yr^{-1})	μ_b (mas yr^{-1})	v_{l*} (km s^{-1})	v_b (km s^{-1})
model pulsar-screen velocity	-5.30 ± 1.11	61.97 ± 1.11	-56.45	22.23	$\cdots$	$\cdots$
VLBI pulsar proper motion	2.16 ± 0.19	51.64 ± 0.13	-46.69	28.02	-137.24	82.34
Screen motion	$\cdots$	$\cdots$	9.76	5.79	18.00	10.68

Table 5. Summary of velocities in the double-refraction model. The velocities listed in equatorial coordinates are the relative velocity in heliocentric system, while the velocities in Galactic coordinates are the relative velocities in LSR (Local Standard of Rest). $\mu_{\alpha*} = \Delta\alpha\cos(\delta)/t$ and $\mu_{l*} = \Delta l\cos(b)/t$, for which we move the center position from $(\Delta\alpha, \Delta\delta)$ or (l, b) to (0,0). v_{l*} and v_b are the linear velocities relative to the LSR. The screen is only moving slowly (~ 21 km s^{-1}). Ellipses reflect the unobserved and frame dependent parameters.
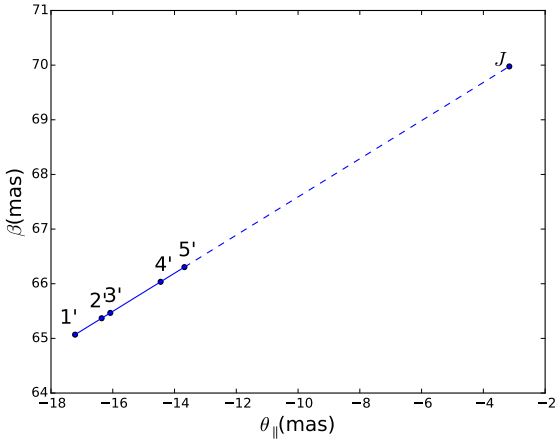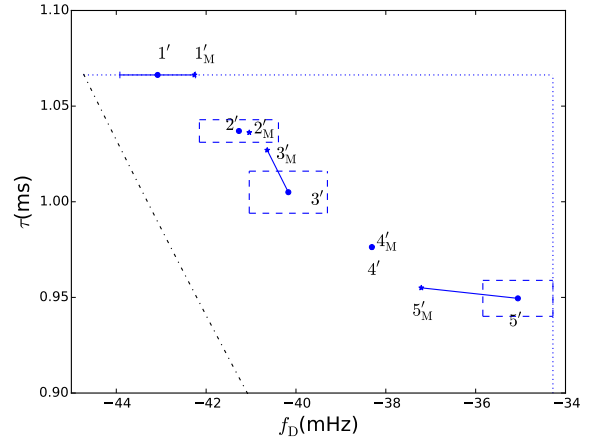

Figure 11. Deflection angle $\beta = \pi - \angle AHB$ on lens 2. Point J denotes the expected position to form a single refraction image, which is not observed. The small change in angle relative to the observed images precludes a finite refraction cut-off, since the data spans 10 per cent bandwidth, with a 20 per cent change in refractive strength. We propose a swallowtail caustic as the likely origin for the termination of the second lens sheet.

Figure 12. Model comparison. Points with subscripts are derived from the double-refraction model, see Table 4. Rectangles mark the 1-σ error region. Points 1' (only for τ) and 4' are used to fit the model, and thus do not have an error region. The rectangles cover 10^{-3} of the area in the dotted region bounded by the parabolic arc and the data points. We interpret this precise agreement between model and data is unlikely to be a random coincidence.

overlaid on point H_5; and on 2005 August 26, which is 78 days before the observation, the lensed image would have appeared overlayed on point H_1. The model predicts the presence of a singly-refracted image refracted at these points, in addition to the doubly-refracted images.

The generic flux of a lensed image is the ratio of the lens transverse size to maximum impact parameter (Pen & King 2012). Near the caustic, the lensed flux can become very high. The 1-ms group is about a factor of 4 fainter than the 0.4-ms group. The high flux of the second caustic suggests it to be relatively wide, perhaps a fraction of an AU. Due to the odd image theorem, one generically expects two distinct sets of double lensed arcs. We only see one (generically the outer one), which places an upper bound on the brightness of the inner image. In a divergent lens(Clegg et al. 1998), the inner image is generically much fainter, so perhaps this is not surprising. For a convergent Gaussian lens, the two images are of similar brightness, but a more cuspy profile will also result in a faint inner image. In gravitational lensing, the odd image theorem is rarely seen to hold, which is generally thought to be due to one lens being very faint.

One can try to estimate the chance of accidental agreement between model and data. We show the data visually in Fig. 12.

To estimate where points might lie accidentally, we conservatively compare the area of the error regions to the area bounded by the parabola and the data points, as shown by dotted lines. This results in about 10^{-3}, suggesting that the model is unlikely to be an accidental fit.

It might be a good supplementary study to conduct a multi-screen simulation that provides ray tracing through a large number of inclined sheets. By adjusting the parameters, we can test the possibility of multi-refractions. However, this is obviously beyond the scope of the current paper.

3.4 Distance degeneracies

With two lens screens, the number of observables increases: in principle one could observe both single refraction delays and angular positions, as well as the double reflection delays and angular positions. Three distances are unknown, equal to the number of observables. Unfortunately, these measurements are degenerate, which can be seen as follows. From the two screens $i = 1, 2$, the two single deflection effective distance observables are $D_{ie} \equiv 2c\tau_i/\theta_i^2 = D_i^2(1/D_i + 1/D_{\text{p}i})$. A third observable effective distance is that of screen 2 using screen 1 as a lens, $D_{21\text{e}} = D_1^2(1/D_1 + 1/D_{21})$, within the triangle that is formed by lens 1, lens 2 and the observer.
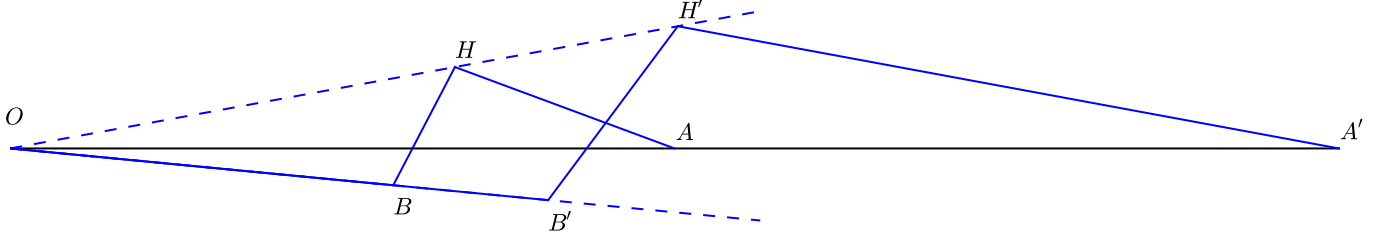
Figure 13. Illustration of double-refraction degeneracy. As in Fig. 5, all observables are identical for both the prime and un-primed geometries, including all pairwise delays and angular positions. This degeneracy also holds in three dimensions.

That is also algebraically derivable from the first two relations: $D_{21e} = D_{1e}D_{2e}/(D_{2e} - D_{1e})$. We illustrate the light path in Fig. 13.

In this archival data set, the direct single lens from the further plane at position J is missing. It would have been visible 59 days earlier. The difference in time delays to image J and the double reflection images would allow a direct determination of the effective distance to lens plane 2. Due to the close to 90° angle $\angle\ DAJ$ between lenses, the effect would be about a factor of 10 ill conditioned. With sufficiently precise VLBI imaging one could distinguish if the doubly-refracted images are at position B (if lens 1 is closer to the observer) or position H (if lens 2 is closer to the observer). As described above, we interpret the effective distances to place screen 2 further away.

4   DISCUSSIONS

4.1   Interpretation

The relative motion between pulsar and lens is directly measured by the differential frequency, and is not sensitive to details of this model. B10 derived similar motions. This motion is in broad agreement with direct VLBI proper motion measurement, requiring the lens to be moving slowly compared to the pulsar proper motion or the LSR. The lens is ~ 200 pc above the Galactic disk. Matter can either be in pressure equilibrium, or in free-fall, or some combination thereof. In free fall, one expects substantial motions. These data rule out retrograde or radially Galactic orbits and indicate that the lens is co-rotating with the Galaxy. In pressure equilibrium, gas rotates slower as its pressure scale height increases, which appears consistent with the observed slightly slower than co-rotating motion. The modest lens velocities also appear consistent with the general motion of the ISM, perhaps driven by Galactic fountains (Shapiro & Field 1976) at these latitudes above the disk. In the inclined sheet model, the waves move at Alfvénic speed, but due to the high inclination, they will move less than one percent of this speed in projection on the sky, and thus be completely negligible compared to other sources of motion.

Alternative models, for example, evaporating clouds (Walker & Wardle 1998) or strange matter (Pérez-García et al. 2013), do not make clear predictions. One would expect higher proper motions from these freely orbiting sources, and larger future scintillation samples may constrain these models.

Inclining one sheet randomly to better than 1 per cent requires of order 10^4 randomly placed sheets, i.e. many per parsec. This sheet extends for ~ 10 AU in projection, corresponding to a physical scale greater than 1000 AU. These two numbers roughly agree, leading to a physical picture of magnetic domain boundaries every ~ 0.1 pc. B0834+06 has had noted arcs for multiple years, perhaps suggesting this dominant lens plane is larger than typical. One might expect to reach the end of the sheet within decades.

A generic prediction of the inclined sheets model is a change in rotation measure across the scattering length. Over 1000 AU, one might expect a typical RM (rotation measure) change of 10^{-3} rad/m^2. At low frequencies, for example in LOFAR[1] or GMRT[2], the size of the scattering screen extends another order of magnitude in angular size, and the RM in different lensed images are different, increasing to ~ 0.01, which is plausibly measurable. Even for an unpolarized source, the left and right circularly polarized (LCP, RCP) dynamic spectra will be slightly different. Usually a secondary spectrum (SS) is formed by Fourier transforming the dynamic spectrum and multiplying by its complex conjugate. To measure the RM, one multiplies the Fourier transform of the LCP dynamic spectrum by the complex conjugate of the RCP Fourier transform. This will display a phase gradient along the Doppler frequency axis. In the SS, each pixel is the sum of correlations of pairs of scattering points with corresponding lag and Doppler velocity. The velocity is typically linear in the pair separation, which is also the case for differential RM. This statistic is analogous to the cross gate secondary spectrum as applied in Pen et al. (2014).

4.2   Possible improvements

We discuss several strategies which can improve on the solution accuracy. The single biggest improvement would be to monitor the speckle pattern over several months, as the pulsar crosses each individual lens, including both lensing systems. This allows a direct comparison of single-refraction to double-refraction arclets.

Angular resolution can be improved using longer baselines, for example adding a GMRT-GBT baseline doubles the resolution. Observing at multiple frequencies over a longer period allows for a more precise measurement: when

---

[1] http://www.lofar.org/
[2] http://gmrt.ncra.tifr.res.in/

the pulsar is between two lenses, the refraction angle β is small, and one expects to see the lensing at higher frequency, where the resolution is higher, and distances between lens positions can be measured to much higher accuracy.

Holographic techniques (Walker et al. 2008; Pen et al. 2014) may be able to measure delays, fringe rates, and VLBI positions substantially more accurately. Combining these techniques, the interstellar lensing could conceivably achieve distance measurements an order of magnitude better than the current published effective distance errors. This could bring most pulsar timing array targets into the coherent timing regime, enabling arc minute localization of gravitational wave sources, lifting any potential source confusion.

Ultimately, the precision of the lensing results would be limited by the fidelity of the lensing model. In the inclined sheet model, the images move along fold caustics. The straightness of these caustics depends on the inclination angle, which in turn depends on the amplitude of the surface waves. This analysis indicates a high degree of inclination, and thus high fidelity for geometric pulsar studies.

5   CONCLUSIONS

We have applied the inclined sheet model (Pen & Levin 2014) to archival apex data of PSR B0834+06. The data are well-fit by two linear lensing screens, with nearly planar geometry. The second screen provides a precision test with 10 observables (5 time delays and 5 differential frequencies) and 3 free parameters (the marked points in Table 4). The model fits the data to $\sim$ percent accuracy on each of 7 data points. This natural consequence of very smooth reconnection sheets is an unlikely outcome of ISM turbulence. These results, if extrapolated to multi-epoch observations of binary systems, might result in accurate distance determinations and opportunities for removing scattering induced timing errors. This approach also opens the window to measuring precise transverse motions of the ionized ISM outside the Galactic plane.

6   ACKNOWLEDGEMENTS

REFERENCES

Arnold V. I., 1990, Singularities of Caustics and Wave Fronts. Springer Netherlands
Boyle L., Pen U.-L., 2012, Phys. Rev. D, 86, 124028
Braithwaite J., 2015, MNRAS, 450, 3201
Brisken W. F., Macquart J.-P., Gao J. J., Rickett B. J., Coles W. A., Deller A. T., Tingay S. J., West C. J., 2010, ApJ, 708, 232
Clegg A. W., Fey A. L., Lazio T. J. W., 1998, ApJ, 496, 253
Cordes J. M., Rickett B. J., Stinebring D. R., Coles W. A., 2006, The Astrophysical Journal, 637, 346
Deller A. T., Archibald A. M., Brisken W. F., Chatterjee S., Janssen G. H., Kaspi V. M., Lorimer D., Lyne A. G., McLaughlin M. A., Ransom S., Stairs I. H., Stappers B., 2012, ApJ, 756, L25
Deller A. T., Boyles J., Lorimer D. R., Kaspi V. M., McLaughlin M. A., Ransom S., Stairs I. H., Stovall K., 2013, ApJ, 770, 145
Efron B., Tibshirani R., 1991, Science, 253, 390
Goldreich P., Sridhar S., 2006, ApJ, 640, L159
Hill A. S., Stinebring D. R., Barnor H. A., Berwick D. E., Webber A. B., 2003, The Astrophysical Journal, 599, 457
Kramer M., Stairs I. H., Manchester R. N., McLaughlin M. A., Lyne A. G., Ferdman R. D., Burgay M., Lorimer D. R., Possenti A., D'Amico N., Sarkissian J. M., Hobbs G. B., Reynolds J. E., Freire P. C. C., Camilo F., 2006, Science, 314, 97
Longuet-Higgins M. S., 1960, J. Opt. Soc. Am., 50, 845
Lorimer D. R., Kramer M., 2012, Handbook of Pulsar Astronomy. Cambridge University Press
Pen U.-L., King L., 2012, MNRAS, 421, L132
Pen U.-L., Levin Y., 2014, MNRAS, 442, 3338
Pen U.-L., Macquart J.-P., Deller A. T., Brisken W., 2014, MNRAS, 440, L36
Pérez-García M. Á., Silk J., Pen U.-L., 2013, Physics Letters B, 727, 357
Shapiro P. R., Field G. B., 1976, ApJ, 205, 762
Stinebring D. R., McLaughlin M. A., Cordes J. M., Becker K. M., Goodman J. E. E., Kramer M. A., Sheckard J. L., Smith C. T., 2001, ApJ, 549, L97
Walker M., Melrose D., Stinebring D., Zhang C., 2004, Monthly Notices of the Royal Astronomical Society, 354, 43
Walker M., Wardle M., 1998, ApJ, 498, L125
Walker M. A., Koopmans L. V. E., Stinebring D. R., van Straten W., 2008, MNRAS, 388, 1214